RSC Advances

PAPER

View Article Online
View Journal | View Issue

Open Access Article. Published on 13 January 2026. Downloaded on 3/10/2026 7:01:37 PM.
This article is licensed under a Creative Commons Attribution-NonCommercial 3.0 Unported Licence.

Check for updates

Cite this: *RSC Adv.*, 2026, **16**, 2702

Received 7th November 2025
Accepted 2nd January 2026

DOI: 10.1039/d5ra08571c

rsc.li/rsc-advances

Cholesterol tunes lipid bilayer interactions

Wei Liu,[a] Jinwei Zhong,[a] Pui Wo Felix Yeung,[b] Xiahui Xiao,[a] Zuwei Zhao,[a] Hang Jiang,[a] Yuwei Zhu *[a] and To Ngai *[b]

In this study, we prepared SLBs on polystyrene colloids (CSLBs) and planar glass substrates with tunable cholesterol content. Using a fixed DPPC : DOPC molar ratio of 3 : 1 to promote the phase separation, we observed pronounced heterogeneity in CSLB diffusion near planar membranes. Notably, by profiling interbilayer interaction potentials, we found that cholesterol concentrations of ∼11 and ∼30 mol% significantly enhance bilayer adhesion—likely through membrane fusion intermediates. These findings highlight cholesterol's critical role in modulating interbilayer mechanics.

1 Introduction

Accumulating evidence highlights the pivotal role of cholesterol in regulating the biophysical properties of cellular membranes, particularly in processes involving membrane fusion.[1–3] Cholesterol primarily reduces membrane fluidity and permeability by rigidifying the fluid phase of lipid bilayers.[4,5] In addition, it enhances membrane stability and increases the bending modulus, promoting negative curvature that serves as a structural precursor to fusion events.[6,7] Through these effects, cholesterol is thought to modulate a range of critical cellular processes, including immune signalling,[8] host–pathogen interactions,[9] cancer development and progression,[10] and cardiovascular disease.[11]

Cellular membranes exhibit intrinsic spatiotemporal dynamics and are characterized by lateral and temporal heterogeneity at sub-microscopic scales. This heterogeneity, and its physiological relevance, has been closely associated with the lipid raft hypothesis,[12] which posits the emergence of liquid–liquid phase separation (LLPS) within lipid bilayers. According to this framework, affinity–driven interactions and preferential associations between cholesterol and saturated lipids facilitate the formation of relatively ordered microdomains with reduced fluidity. These liquid-ordered (L_o) phases, enriched in hydrophobic components, promote key cellular processes such as signalling and trafficking, particularly *via* lipidated proteins and glycosylphosphatidylinositol (GPI)-anchored proteins.[13] A previous study reported that approximately 35% of plasma membrane proteins localize within the L_o phase.[14] Given the critical role of these phase-separated raft nanodomains (typically 10–200 nm) that have the potential to form microdomains (>300 nm) in mediating lipid–lipid and lipid–protein interactions, a range of biophysical model systems—including lipid monolayers, supported lipid bilayers (SLBs), micro/nanoscopic liposomes, and giant unilamellar vesicles (GUVs)—have been employed to investigate LLPS and the underlying principles of lipid raft formation.[15–18]

State-of-the-art techniques—including super-resolution optical microscopy (*e.g.*, PALM, STED, and STORM),[19–21] single-molecule fluorescence tracking,[22–28] fluorescence correlation spectroscopy,[29–34] Förster resonance energy transfer (FRET),[35–39] and quartz crystal microbalance with dissipation monitoring (QCM-D)[40,41]—have been employed to probe nanoscale structures, membrane heterogeneity, and lateral diffusion of membrane components. These methodologies have provided compelling evidence for the structural and dynamic characteristics of cholesterol-enriched domains. In addition, simulations serve as powerful tools for probing biomolecular diffusivity, phase separation, membrane fusion, and vesicle–membrane interactions.[2,7,42–54] Recent systematic molecular dynamics studies have revealed that membrane fusion is facilitated when lipid bilayers are enriched in cholesterol, whereas fusion is markedly reduced when both the vesicle and planar membrane are cholesterol-rich.[7] Another study further demonstrated that elevating the cholesterol content of exosome membranes enhances their cellular uptake *via* fusion with the plasma membrane.[2] Collectively, these theoretical investigations highlight the critical role of cholesterol in regulating the biofunctions of cellular membranes.

However, direct quantification of cholesterol's impact on interbilayer interactions remains a fundamental challenge. Neutron and X-ray reflectivity experiments have been widely employed to probe the attractive interactions between fully charged lipid bilayers, as well as to quantify key physical properties such as bending modulus, orientational order parameters, and membrane curvature during fusion events.[6,55–57] In addition, Bevan and co-workers utilized total internal reflection microscopy (TIRM) to directly measure the

[a]*The Key Laboratory of Synthetic and Biological Colloids, Ministry of Education & School of Chemical and Material Engineering, Jiangnan University, Wuxi 214122, P.R. China. E-mail: uvyzhu@gmail.com*

[b]*Department of Chemistry, The Chinese University of Hong Kong, Shatin, N.T., Hong Kong 999077, P.R. China. E-mail: tongai@cuhk.edu.hk*

© 2026 The Author(s). Published by the Royal Society of Chemistry

Open Access Article. Published on 13 January 2026. Downloaded on 3/10/2026 7:01:37 PM.
This article is licensed under a Creative Commons Attribution-NonCommercial 3.0 Unported Licence.

kT-scale interactions between silica colloids modified with SLBs of varying compositions (*e.g.*, PEGylated *vs.* non-PEGylated).[58] Their findings demonstrated that colloid size and the extent of SLB PEGylation jointly dictate the balance between colloidal aggregation and SLB fusion, thereby highlighting the interplay between colloidal surface chemistry and bilayer stability. A deeper understanding of the underlying physical principles governing membrane–membrane interactions could pave the way for the rational design of lipid vesicle-based drug delivery systems and next-generation gene therapies.

In this study, we aimed to answer, at least in part, how cholesterol tunes the inter-bilayer interactions by a direct measurement using TIRM (Fig. 1). We prepared the SLBs on 3 μm polystyrene colloids and planar glass substrates with tunable cholesterol content. The bilayers consisted of saturated DPPC and unsaturated DOPC at a fixed molar ratio of 3 : 1. This composition was specifically selected to promote LLPS across a broad cholesterol concentration range (approximately 15–50 mol%), as supported by previous literature.[59] We demonstrated that cholesterol content can significantly modulate the diffusivity of colloidal-supported lipid bilayers near planar membranes, with notably enhanced interfacial adhesion observed at approximately 11 and 30 mol% cholesterol.

2 Experimental

2.1. Preparation of liposomes

Liposomes were prepared using saturated 1,2-dipalmitoyl-*sn*-glycero-3-phosphocholine (DPPC, 99%, Macklin), unsaturated 1,2-dioleoyl-*sn*-glycero-3-phosphocholine (DOPC, >99%, Aladdin) and cholesterol (≥99%, Macklin) based on an established protocol.[60] In typical experiments, cholesterol (0.3867 g) was dissolved in 1 mL of a mixed organic solvent (cyclohexane/ethanol = 19/1, v/v) to prepare a stock solution at a concentration of 1.0 mmol mL^{-1}. 0.01 g DPPC and 0.0035 g DOPC were dissolved in the mixed solvent to prepare a solution at desired concentrations. Lipid samples were dissolved with ultrasonic assistance to yield liposome solutions at a final concentration of 2 mM. To remove impurities, each sample was filtered three times through a 0.22 μm Nylon membrane filter.

2.2. Cleaning of glass plates

Glass slide (25 × 75 × 1 mm, Fisher Scientific) was immersed in piranha solution (H_2SO_4/H_2O_2 = 3/1, v/v) for 2 h and then washed with D. I. H_2O for 10 times to remove the excess piranha solution. Subsequently, the slide was sequentially washed with D. I. H_2O, absolute ethanol, and D. I. H_2O, each for 15 min through ultrasonication. The cleaned slide was treated with plasma (PDC-002, Harrick Plasma, USA) for 3 min to obtain a superhydrophilic surface.

2.3. Preparation of planar supported lipid bilayers

Supported lipid bilayers (SLBs) were prepared through the Langmuir–Blodgett (LB) technique (Fig. 2).[61] Lipid stock solutions were spread at the air–water interface of a LB trough (Microtrough G2, Kibron, Finland), making the surface pressure to be 1 mN m^{-1} after calibration, and the interface was allowed to equilibrate for 30 min. The lipid monolayer was compressed at 10 mm min^{-1} until the surface pressure reached ~40 mN m^{-1}, and then transferred to the glass substrate by vertical deposition at a pulling rate of 2 mm min^{-1}. The second monolayer was spread and compressed in the same way as the one for the first layer, then deposited on the coated surface by dipping the substrate into the subphase at a rate of 2 mm min^{-1}. The lipid bilayer-coated glass was transferred using a polytetrafluoroethylene (PTFE) mold, during which the lipid bilayer was maintained in an aqueous environment.

2.4. Preparation of colloidal supported lipid bilayers

12 μL lipid solution was dried under nitrogen to form a thin film. After drying, 1 mM NaCl solution was added, and the sample was sonicated for 5 min to disperse the lipids. The mixture was incubated in a 60 °C water bath for 1 h to form vesicles. Polystyrene (PS) particles (8 w/w%, 3.1 μm, Thermo

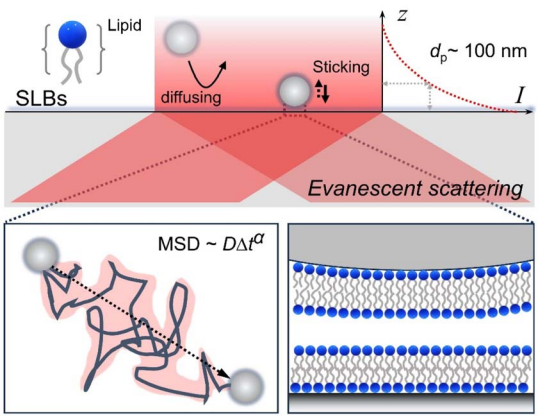

Fig. 1 Schematic illustration of the confined motion of colloidal-supported lipid bilayers near a bio-interface by evanescent scattering with a penetration depth of d_p ~100 nm.

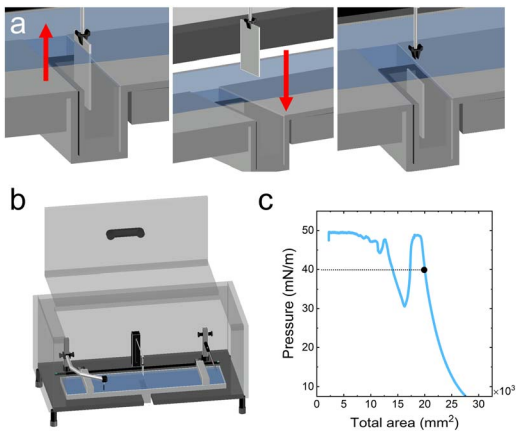

Fig. 2 Preparation of the supported lipid bilayers on a glass substrate through the Langmuir–Blodgett technique. (a) Dipping the substrate into the subphase to obtain lipid monolayer and bilayer. (b) Langmuir–Blodgett trough. (c) Compression isotherms.

Open Access Article. Published on 13 January 2026. Downloaded on 3/10/2026 7:01:37 PM.
This article is licensed under a Creative Commons Attribution-NonCommercial 3.0 Unported Licence.

Fisher Scientific) was added into the solution. After 30 min of incubation, the sample was shaken for 30 min to yield lipid bilayer-coated particle surfaces (colloidal-supported lipid bilayers, CSLBs). Above the phase transition temperature, lipid molecules become more fluid-like and loosely packed, facilitating bilayer formation on the particle surface.

2.5. Observation of lipid monolayer and bilayer

To visualize lipid monolayer/bilayer under confocal fluorescent microscopy, 1 wt% fluorescent lipid, NBD PC (Avanti) was added in the lipid solution. The lipid monolayer and bilayer were prepared on the glass substrate through LB technique and on particle surfaces as aforementioned. The as-prepared lipid monolayer and bilayer were observed using a confocal laser fluorescent microscope (Eclipse Ti2, Nikon Inc., JP) at the exciting wavelength of 488 nm (Fig. 3). The lipid bilayer was maintained in an aqueous environment during the experiment.

2.6. Total internal reflection microscopy

To form an evanescent field at the glass/water interface, a HeNe laser with a wavelength $\lambda = 632.8$ nm (HeNe Laser, Red, 633 nm, Newport Corporation, USA) was employed in our setup. The intensity of scattering light I exponentially decays with a separation distance h from the interface, expressed as[62]

$$I(h) = I_0 e^{-h/d_p} \tag{1}$$

where I_0 is the maximum scattering intensity of the particles that have reached the surface and d_p is the penetration depth, expressed as

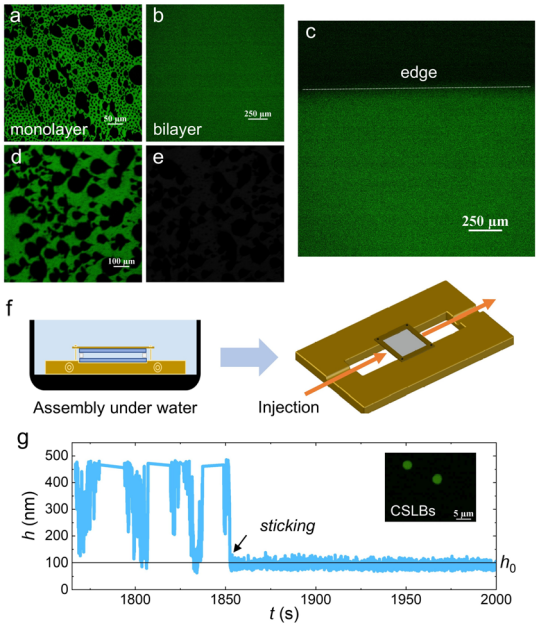

Fig. 3 Confocal images of as-prepared lipid monolayer (a) and supported lipid bilayer (b) on glass substrates before (d) and after (e) wiping by EtOH. (c) Edge region of the supported lipid bilayer. (f) Flowing chamber assembled under water to maintain the integrity of SLBs. (g) Height trajectory of single CSLBs to indicate a sticking behavior at ~1850 s. Inset: confocal image of the CSLBs.

$$d_p = \lambda \Big/ \left[4\pi\sqrt{(n_1 \sin\theta)^2 - n_2^2}\right] \tag{2}$$

where λ is the laser wavelength, θ is the incident angle, n_1 and n_2 are the refractive indexes of prism (material: N-BK7) and sample solutions (*i.e.*, aqueous solutions), respectively. Based on the Boltzmann statistics, the particle–surface interactions can be calculated from the position distribution of a fluctuating particle along the z direction, given by[62–64]

$$p(h) = A e^{\frac{-\phi(h)}{kT}} \tag{3}$$

where A is a normalization constant related to the total number of height observations, ϕ is the interaction potential, $p(h)$ is the probability of finding a particle at a certain height, k is the Boltzmann constant, and T is the temperature. Instead of measuring an absolute value of the interaction potential, the potential measured with TIRM is usually a comparative value, given by

$$\frac{\phi(h) - \phi(h_{ref})}{kT} = \ln\frac{p(h_{ref})}{p(h)} \tag{4}$$

where h_{ref} is often chosen as h_m, which represents the separation distance with the lowest potential energy.

2.7. Image acquisition and data processing

A high-speed back-illuminated sCMOS camera (Kinetix22, 2400 × 2400 6.5 μm pixels, Teledyne Photometrics Inc., Tucson, US) in liquid-cooling mode was utilized to capture the TIR-scattering image sequences. A 40× objective (CFI Super Plan Fluor ELWD, NA/WD: 0.6/3.6 mm) mounted on an upright microscope (ECLIPSE FN1, Nikon Inc., JP) was used for imaging. The effective pixel size, l_{pix}, was determined to be ~0.16 μm. Typically, an image sequence of $N = 100\,000$ frames in size of 256 × 256 pixels in 16 bits was captured at an exposure time of 10 ms, referring to a frame rate of 100 fps.

Before TIRM measurements, the background intensity and the maximum intensity I_0 corresponding the zero height for 3.1 μm PS letax microspheres were determined. The setup was calibrated by standard NaCl solutions to ensure the accuracy. In the experiments, two microscopic glass plates sandwiched by a silicone O-ring were employed to construct a flowing cell with 1 mm chamber height. Solutions of CSLBs were injected into the flowing cell through a micro-injection pump (1 mL min^{-1}, SPLab02, Tansoole). CSLBs were allowed to equilibrate for ~20 min before image capturing. The images were processed based on the radial symmetry method under particle-tracking framework using previously reported MATLAB program.[65]

2.8. The diExp elastic model

For particles stuck on the substrate surface, non-DLVO forces—such as hydrophobic interaction and hydration force—turn to be dominated in the intersurface potentials, thus the DLVO theory is not applicable. Accordingly, we use a modified Hookean spring model in an asymmetric shape to describe the potential wells, namely, the diExp elastic model, which is expressed as[66]

 © 2026 The Author(s). Published by the Royal Society of Chemistry

Open Access Article. Published on 13 January 2026. Downloaded on 3/10/2026 7:01:37 PM.
This article is licensed under a Creative Commons Attribution-NonCommercial 3.0 Unported Licence.

$$U(h) = \begin{cases} y_0 + A_0\left(\dfrac{x_c - h}{w_1}\right)^{p_1}, & \text{if } h < x_c \\ y_0 + A_0\left(\dfrac{h - x_c}{w_2}\right)^{p_2}, & \text{if } h > x_c \end{cases} \quad (5)$$

where y_0 denotes the offset determined by the baseline of zero potential, A_0 denotes the amplitude describing the elastic strength for the potential wells, w_1 and w_2 correspond to the full width at half maximum (FWHM) on the left and right side of the potential wells, and p_1 and p_2 correspond to the compressed and stretched elastic exponents, respectively. Under this criterion, the effective elastic coefficient, k_{eff}, acts as an estimate describing the intersurface interaction for stuck particles with soft boundaries, which can be given as

$$k_{\text{eff}} \sim (w_1^{p_1} w_2^{p_2})^{-1/2} \quad (6)$$

3 Results and discussion

3.1. Near-wall confined motion of CSLBs

Using total internal reflection microscopy, we first observed pronounced heterogeneity in the diffusive behavior of CSLBs near planar membrane surfaces (Fig. 4). This technique leverages evanescent scattering to enable high-precision tracking of kT-scale interactions between colloids and flat interfaces along the z-axis (normal to the surface). Detailed methodology is provided in our recent publication and other literature.[66,67] Quantitative analysis revealed that the diffusion range of CSLBs initially increases with cholesterol content, reaching a maximum at approximately 27 mol% ($x = 1.5$), followed by a sharp decline (Fig. 5a). Coincidentally, the diffusion range under strictly-confined motion (*e.g.*, $x = 0$, 0.5, 1.75 and 2) corresponded to the size of the phase-separated raft domains (~200–300 nm). To further characterize this behavior, we

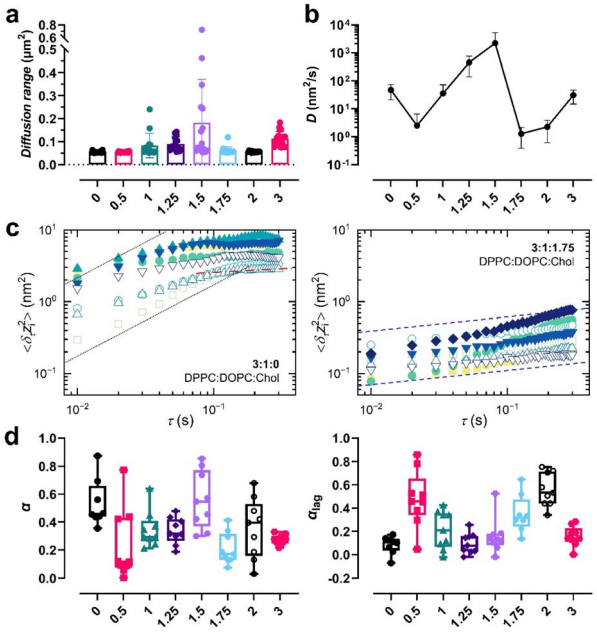

Fig. 5 Diffusive behavior of the colloidal-supported lipid bilayers (CSLBs) modulated by cholesterol content. (a) Diffusion range of CSLBs. (b) Diffusion coefficients in the z-direction. Lipid compositions were fixed at a DPPC : DOPC : cholesterol molar ratio of 3 : 1 : x, with cholesterol fraction x indicated along the bottom axis. (c) Representative MSD curves of CSLBs at varying cholesterol levels. The dotted (black), dash-dotted (red), and dashed (blue) lines correspond to power-law indices α of 1, 0.1, and 0.2, respectively, where MSD $\sim \tau^{\alpha}$. (d) Power-law index α extracted from short-time (left panel) and long-time (right panel) MSD measurements.

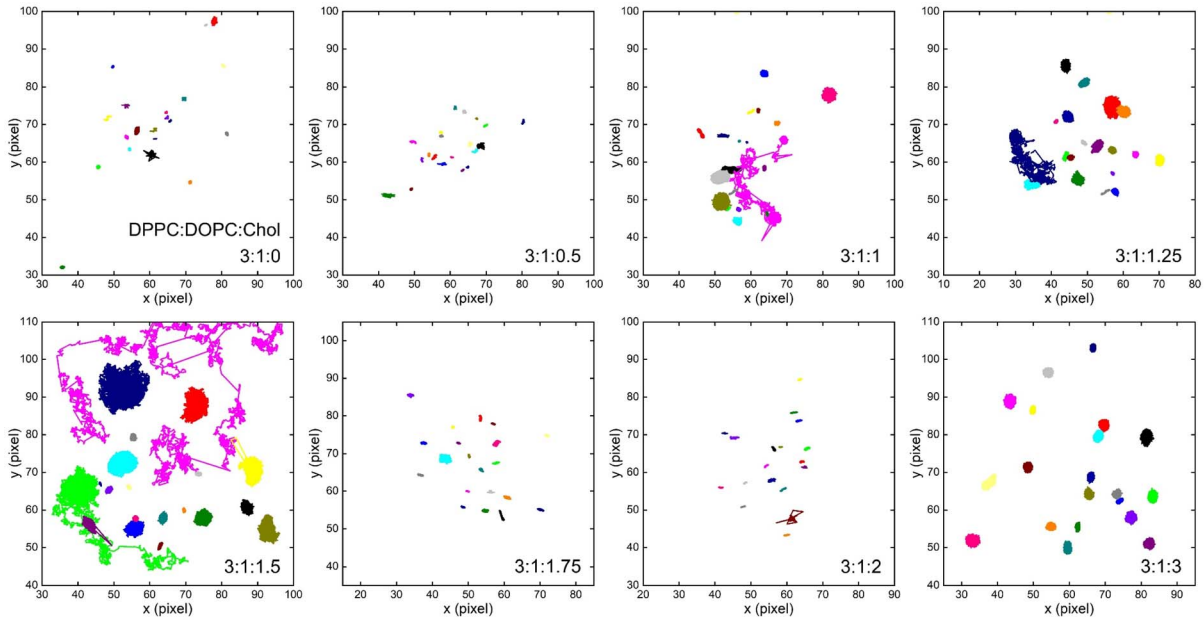

Fig. 4 Representative lateral trajectories of colloidal-supported lipid bilayers (CSLBs) diffusing on planar membranes composed of 3 : 1 DPPC/DOPC, with varying cholesterol content.

Open Access Article. Published on 13 January 2026. Downloaded on 3/10/2026 7:01:37 PM.
This article is licensed under a Creative Commons Attribution-NonCommercial 3.0 Unported Licence.

performed time-averaged mean square displacement (MSD) measurements in three dimensions[44]

$$\overline{\langle \delta_\tau r_i^2 \rangle} = \frac{1}{t-\tau}\int_0^{t-\tau} \left[\vec{r}(t'+\tau) - \vec{r}(t')\right]^2 \mathrm{d}t' \quad (7)$$

where $\vec{r}(t)$ denotes the position of the tracked CSLBs and $\tau \ll t$ is the lag time. After correcting for particle positional errors, a linear fit to the MSD yielded the diffusion coefficient D. Notably, two distinct minima in the z-directional diffusion coefficient ($D \approx 1.5$–$2\ \mathrm{nm^2\ s^{-1}}$) were observed at ~11 and 30 mol% cholesterol, indicating strong confinement (Fig. 5b). Consistent with this, we detected extremely weak fluctuations in the corresponding z-directional displacements (data not shown). Furthermore, we confirmed that the observed low diffusivity was not solely attributable to near-wall hindrance effects (see height profile in Fig. 7a). These findings suggest that high-curvature lipid-stalk or hemifusion intermediates may form under these conditions, contributing to the observed confinement.

3.2. Anomalous diffusion of CSLBs

Substantial heterogeneity in the diffusivity of individual CSLBs was revealed through the broad distributions of MSD and the power-law index α, where MSD scales as $\sim\tau^\alpha$) (Fig. 5c and d). In classical diffusion, MSD exhibits a linear dependence on lag time, *i.e.*, MSD $\sim 2D\tau$, with the diffusion coefficient D determined solely by the viscosity of a homogeneous environment. However, anomalous or subdiffusive behavior is commonly observed in biological systems, such as the lateral diffusion of transmembrane proteins on cellular membranes.[44] Analogously, we observed widespread transient subdiffusion of CSLBs on membrane surfaces across a broad range of cholesterol content ($x \sim 0$–3), as indicated by MSD analysis. Interestingly, the power-law index α derived from short lag times exhibited a strong positive correlation with D, whereas the index obtained from longer lag times (α_{lag}) showed an inverse trend with D as a function of x. Compared to long-time measurements, short-time diffusivity is inherently more variable, reflecting dynamic heterogeneity in the local environment and transient interactions.[68] This inverse relationship between short- and long-time diffusivity suggests a breakdown of ergodicity in the time-dependent diffusion process of CSLBs on membranes.[69]

3.3. Interbilayer interactions

The observed diffusive properties revealed abnormal adhesion behavior—manifested as extremely low diffusivity—of CSLBs on bilayer membranes at specific cholesterol concentrations (~11

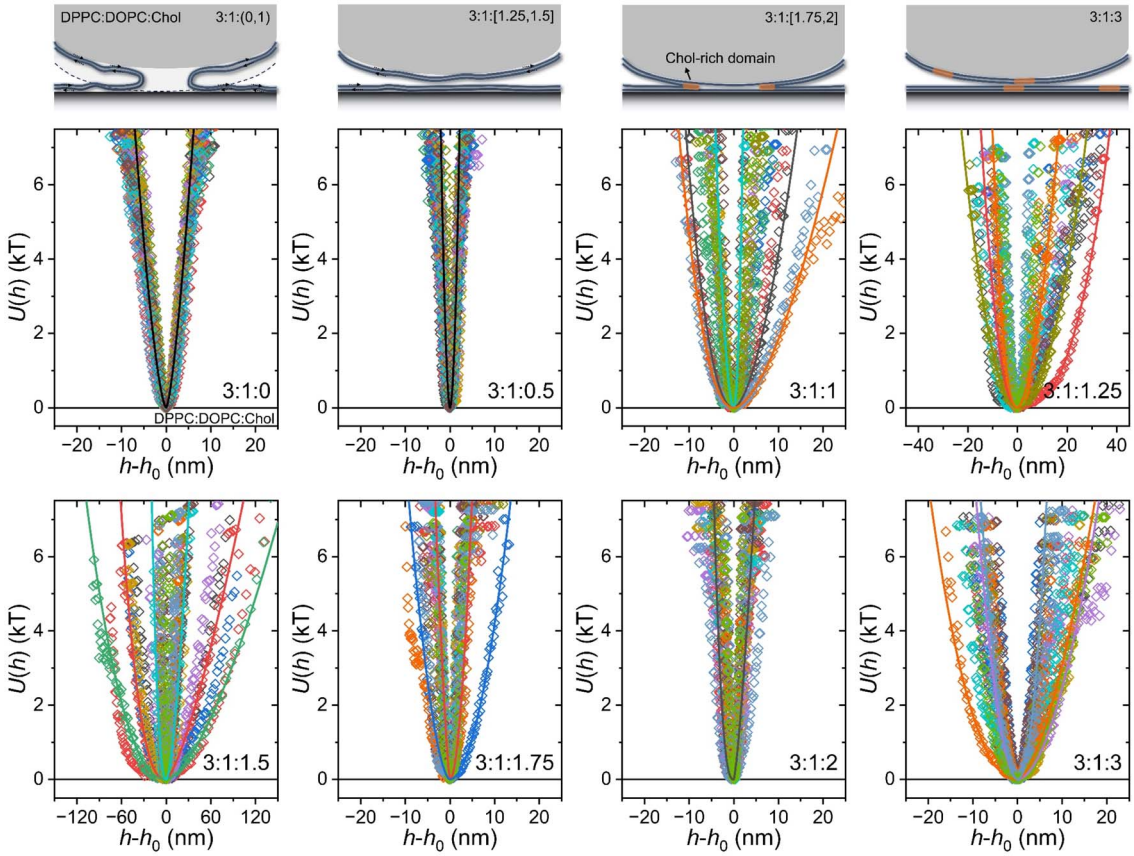

Fig. 6 Interbilayer potential energy profiles $U(h - h_0)$ at varying cholesterol contents. Representative solid lines correspond to fits using the diExp elastic model. Top panel: Schematic illustration of the configuration and fusion process between colloidal-supported lipid bilayers (CSLBs) and planar bilayers.

 © 2026 The Author(s). Published by the Royal Society of Chemistry

Open Access Article. Published on 13 January 2026. Downloaded on 3/10/2026 7:01:37 PM.
This article is licensed under a Creative Commons Attribution-NonCommercial 3.0 Unported Licence.

and 30 mol%). To further investigate how cholesterol content influences interbilayer interactions, we applied Boltzmann statistics to derive the intersurface potential energy $U(h)$ by transforming the positional distribution of individual fluctuating particles along the z-axis. Fig. 6 presents the interbilayer potential energy profiles, with the equilibrium height h_0 selected as the reference position. The most confined diffusion corresponds to the narrowest potential energy distribution, indicating strong adhesion with a confinement scale of <10 nm at $U = 6kT$. Consistent with our previous observation of asymmetric potential profiles—where single coronated particles diffused on SLBs[66]—we also detected asymmetry in the mechanical coupling of CSLBs. To further interpret this behavior, we applied the diExp elastic model (see Experimental), which yielded potential energy profiles in good agreement with non-DLVO theoretical predictions.

To quantify the adhesion strength between bilayers, we calculated the effective elastic coefficient, k_{eff}, which serves as an estimate of the intersurface interaction for particles exhibiting confined motion under soft boundary conditions. A bimodal distribution of k_{eff} as a function of cholesterol content x was observed (Fig. 7b), consistent with the two minima in the diffusion coefficient. Additionally, Fig. 7c reveals a convergent distribution of the elastic exponents around a value of 2, indicative of Hookean spring-like behavior, regardless of whether the motion is directed toward or away from the wall.

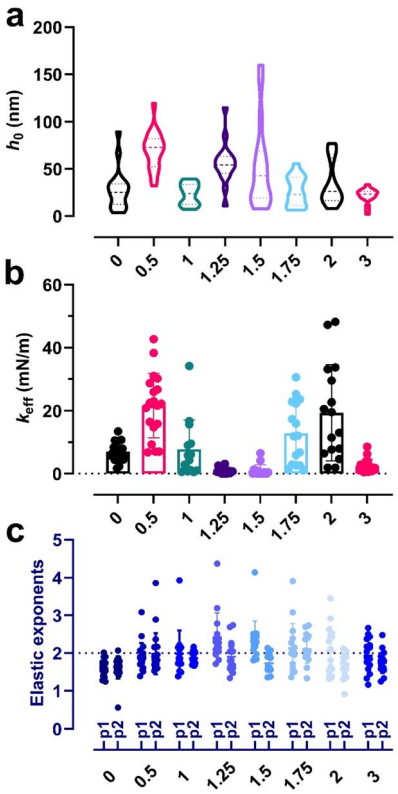

Fig. 7 Quantitative analysis of interbilayer interactions. (a) Distribution of equilibrium height h_0. (b) Effective elastic coefficient k_{eff}. (c) Corresponding elastic exponents for the potential wells shown in Fig. 6.

Notably, the peak value of k_{eff} approaches ~50 mN m^{-1}, approximately three orders of magnitude greater than the adhesion strength observed between protein-coronated particles and SLBs.[66] Such pronounced sticking behavior is unlikely to arise from purely near-field interactions without physical contact.

Therefore, we propose that high-curvature lipid-stalk or hemifusion intermediates[70] may form between the bilayers at the two specific cholesterol contents (*i.e.*, ~11 and 30 mol%), which lie near the phase separation boundaries in the ternary phase diagram[59,71] of the DPPC:DOPC:cholesterol system (see Fig. 6, top panel). At a relatively low cholesterol content ($x \sim 0$–1), an uplifted and flexural fold structure with high internal fluidity is expected accordingly. As cholesterol increases beyond 20 mol%, the bilayer becomes more elastic and structurally stable. Under these conditions, the hydration layer between bilayers may act as a lubricating boundary, facilitating enhanced lateral diffusion at x ~1.5. Further increasing cholesterol content (~30 mol%, x ~1.75–2) likely promotes the formation of cholesterol-rich microdomains (lipid rafts), potentially triggering hemifusion or full fusion events. At extremely high cholesterol levels (*e.g.*, >40 mol%), the membranes become significantly rigidified, suppressing lipid exchange between bilayers; instead, interbilayer bridging *via* lipid rafts may become the dominant interaction mechanism.

4 Conclusions and discussion

Cholesterol is widely recognized as a key regulator of membrane fusion, where its cone-shaped molecular geometry introduces intrinsic negative curvature that promotes stalk formation.[70] For fusion to occur, however, lipid bilayers must first overcome the hydration repulsion barrier imposed by ordered water molecules at the lipid–water interface.[72,73] Recent studies suggest that cholesterol not only contributes negative curvature but also reduces hydration forces, thereby facilitating close membrane apposition and lowering the energetic cost of stalk formation.[74,75] Importantly, the impact of cholesterol is not universal: while it can soften unsaturated lipid membranes, it stiffens saturated bilayers, underscoring its complex role in modulating membrane mobility, curvature sensing, and elasticity.[4,76]

In our system, peak-like adhesion enhancement at ~11 mol% and ~30 mol% cholesterol concentrations in DPPC : DOPC (3 : 1) supported bilayers reveals a nonlinear regulatory effect that resonates with established phase diagram studies of model membranes. Prieto and colleagues have shown that cholesterol drives liquid-ordered (L_o) and liquid-disordered (L_d) phase segregation within specific compositional windows, while suppressing domain formation outside these ranges.[77–82] Such nonlinear behavior is attributed to cholesterol's wedge-like geometry, its modulation of local curvature, and preferential interactions with sphingolipids. We propose that the enhanced adhesion observed at intermediate cholesterol concentrations reflects the stabilization of fusion intermediates through curvature changes in local membrane domains. These findings extend the physicochemical framework of cholesterol

Open Access Article. Published on 13 January 2026. Downloaded on 3/10/2026 7:01:37 PM.
This article is licensed under a Creative Commons Attribution-NonCommercial 3.0 Unported Licence.

action beyond classical DLVO-type interactions, highlighting the combined roles of hydrophobic and hydration forces in shaping membrane mechanics. By situating our results within this broader context, we provide a mechanistic basis for the unexpected nonlinear pattern and open avenues for confirmatory experiments using curvature-sensitive probes or molecular simulations.

In summary, we used total internal reflection microscopy to directly image and measure the near-wall confined diffusion and the *kT*-scale interaction between supported lipid bilayer-modified colloids and planar surfaces. We demonstrated that cholesterol content of approximately 11 and 30 mol% significantly enhance adhesion between lipid bilayers, likely through mechanisms involving membrane phase separation and fusion. These findings highlight the sophisticated role of cholesterol in modulating interbilayer interactions—an open question that remains unresolved. Future work will benefit from direct experimental observations such as FRET, single-particle tracking, Neutron or X-ray scattering and theoretical simulations to further validate the proposed framework, particularly within the DPPC:DOPC:cholesterol system.

Author contributions

Wei Liu: conceptualization, methodology, formal analysis, visualization, supervision, project administration, funding acquisition, writing – original draft. Jinwei Zhong: software, validation, formal analysis, investigation, data curation. Pui Wo Felix Yeung: software, validation, formal analysis. Xiahui Xiao: validation, investigation. Zuwei Zhao: validation, investigation. Hang Jiang: writing – review & editing. Yuwei Zhu: funding acquisition, writing – review & editing. To Ngai: conceptualization, project administration, writing – review & editing.

Conflicts of interest

There are no conflicts to declare.

Data availability

Data will be made available on reasonable request.

Acknowledgements

This work was supported by the National Natural Science Foundation of China (22303033) and the Fundamental Research Funds for the Central Universities, China (JUSRP202501136).

Notes and references

1 E. Sezgin, I. Levental, S. Mayor and C. Eggeling, *Nat. Rev. Mol. Cell Biol.*, 2017, **18**, 361–374.
2 Y. Zhuo, Z. Luo, Z. Zhu, J. Wang, X. Li, Z. Zhang, C. Guo, B. Wang, D. Nie and Y. Gan, *Nat. Nanotechnol.*, 2024, **19**, 1858–1868.
3 A. Mangiarotti, E. Sabri, K. V. Schmidt, C. Hoffmann, D. Milovanovic, R. Lipowsky and R. Dimova, *Nat. Commun.*, 2025, **16**, 1–20.
4 M. Pöhnl, M. F. Trollmann and R. A. Böckmann, *Nat. Commun.*, 2023, **14**, 8038.
5 S. Chakraborty, M. Doktorova, T. R. Molugu, F. A. Heberle, H. L. Scott, B. Dzikovski, M. Nagao, L.-R. Stingaciu, R. F. Standaert and F. N. Barrera, *Proc. Natl. Acad. Sci. U. S. A.*, 2020, **117**, 21896–21905.
6 A. Ivankin and D. Gidalevitz, *Biophys. J.*, 2012, **102**, 293a.
7 C.-P. Chng, K. J. Hsia and C. Huang, *Soft Matter*, 2022, **18**, 7752–7761.
8 A. R. Tall and L. Yvan-Charvet, *Nat. Rev. Immunol.*, 2015, **15**, 104–116.
9 G. A. Kumar, M. Jafurulla and A. Chattopadhyay, *Chem. Phys. Lipids*, 2016, **199**, 179–185.
10 O. F. Kuzu, M. A. Noory and G. P. Robertson, *Cancer Res.*, 2016, **76**, 2063–2070.
11 G. N. Levine, J. F. Keaney Jr and J. A. Vita, *N. Engl. J. Med.*, 1995, **332**, 512–521.
12 K. Simons and E. Ikonen, *Nature*, 1997, **387**, 569–572.
13 M. G. Paulick and C. R. Bertozzi, *Biochem.*, 2008, **47**, 6991–7000.
14 I. Levental, D. Lingwood, M. Grzybek, Ü. Coskun and K. Simons, *Proc. Natl. Acad. Sci. U. S. A.*, 2010, **107**, 22050–22054.
15 J. A. Jackman and N.-J. Cho, *Langmuir*, 2020, **36**, 1387–1400.
16 J. R. Silvius, *Biochim. Biophys. Acta Biomembr.*, 2003, **1610**, 174–183.
17 T. Baumgart, A. T. Hammond, P. Sengupta, S. T. Hess, D. A. Holowka, B. A. Baird and W. W. Webb, *Proc. Natl. Acad. Sci. U. S. A.*, 2007, **104**, 3165–3170.
18 S.-T. Yang, A. J. Kreutzberger, J. Lee, V. Kiessling and L. K. Tamm, *Chem. Phys. Lipids*, 2016, **199**, 136–143.
19 K. Zhanghao, W. Liu, M. Li, Z. Wu, X. Wang, X. Chen, C. Shan, H. Wang, X. Chen and Q. Dai, *Nat. Commun.*, 2020, **11**, 5890.
20 M. B. Stone, S. A. Shelby and S. L. Veatch, *Chem. Rev.*, 2017, **117**, 7457–7477.
21 E. Sezgin, *J. Phys. Condens. Matter*, 2017, **29**, 273001.
22 L. Gascoigne, R. P. Tas, P. G. Moerman and I. K. Voets, *Soft Matter*, 2025, **21**, 3058–3066.
23 G. I. Mashanov, T. A. Nenasheva, A. Mashanova, R. Lape, N. J. Birdsall, L. Sivilotti and J. E. Molloy, *Faraday Discuss.*, 2021, **232**, 358–374.
24 A. Kusumi, Y. M. Shirai, I. Koyama-Honda, K. G. Suzuki and T. K. Fujiwara, *FEBS Lett.*, 2010, **584**, 1814–1823.
25 S. Wieser and G. J. Schütz, *Methods*, 2008, **46**, 131–140.
26 V. Kiessling, J. M. Crane and L. K. Tamm, *Biophys. J.*, 2006, **91**, 3313–3326.
27 K. Ritchie, X.-Y. Shan, J. Kondo, K. Iwasawa, T. Fujiwara and A. Kusumi, *Biophys. J.*, 2005, **88**, 2266–2277.
28 A. Kusumi, C. Nakada, K. Ritchie, K. Murase, K. Suzuki, H. Murakoshi, R. S. Kasai, J. Kondo and T. Fujiwara, *Annu. Rev. Biophys. Biomol. Struct.*, 2005, **34**, 351–378.
29 G.-S. Yang, A. Wagenknecht-Wiesner, B. Yin, P. Suresh, E. London, B. A. Baird and N. Bag, *Biophys. J.*, 2024, **123**, 2256–2270.

 © 2026 The Author(s). Published by the Royal Society of Chemistry

Open Access Article. Published on 13 January 2026. Downloaded on 3/10/2026 7:01:37 PM.
This article is licensed under a Creative Commons Attribution-NonCommercial 3.0 Unported Licence.

30 S. Chiantia, J. Ries and P. Schwille, *Biochim. Biophys. Acta, Biomembr.*, 2009, **1788**, 225–233.
31 J. Ries and P. Schwille, *Phys. Chem. Chem. Phys.*, 2008, **10**, 3487–3497.
32 A. J. García-Sáez and P. Schwille, *Methods*, 2008, **46**, 116–122.
33 A. E. Hac, H. M. Seeger, M. Fidorra and T. Heimburg, *Biophys. J.*, 2005, **88**, 317–333.
34 J. Korlach, P. Schwille, W. W. Webb and G. W. Feigenson, *Proc. Natl. Acad. Sci. U. S. A.*, 1999, **96**, 8461–8466.
35 P. Sharma, R. Varma, R. Sarasij, K. Gousset, G. Krishnamoorthy, M. Rao and S. Mayor, *Cell*, 2004, **116**, 577–589.
36 J. Škerle, J. Humpolíčková, N. Johnson, P. Rampírová, E. Poláchová, M. Fliegl, J. Dohnálek, A. Suchánková, D. Jakubec and K. Strisovsky, *Biophys. J.*, 2020, **118**, 1861–1875.
37 D. F. Ma, C. H. Xu, W. Q. Hou, C. Y. Zhao, J. B. Ma, X. Y. Huang, Q. Jia, L. Ma, J. Diao and C. Liu, *Angew. Chem., Int. Ed.*, 2019, **58**, 5577–5581.
38 Y. Ma, Y. Yamamoto, P. R. Nicovich, J. Goyette, J. Rossy, J. J. Gooding and K. Gaus, *Nat. Biotechnol.*, 2017, **35**, 363–370.
39 M. You, E. Li, W. C. Wimley and K. Hristova, *Anal. Biochem.*, 2005, **340**, 154–164.
40 M. Hanzawa, H. Sugasawa, T. Ogura, K.-i. Iimura and T. Misono, *Phys. Chem. Chem. Phys.*, 2025, **27**, 6858–6866.
41 F. Ruggeri, F. Zhang, T. Lind, E. D. Bruce, B. L. Lau and M. Cárdenas, *Soft Matter*, 2013, **9**, 4219–4226.
42 G. Meher, S. Sinha, G. P. Pattnaik, S. Ghosh Dastidar and H. Chakraborty, *J. Phys. Chem. B*, 2019, **123**, 7113–7122.
43 M. D. Elola and J. Rodriguez, *J. Phys. Chem. B*, 2018, **122**, 5897–5907.
44 E. Yamamoto, T. Akimoto, A. C. Kalli, K. Yasuoka and M. S. Sansom, *Sci. Adv.*, 2017, **3**, e1601871.
45 J. Yang, J. Martí and C. Calero, *Soft Matter*, 2016, **12**, 4557–4561.
46 M. M. Kozlov and L. V. Chernomordik, *Curr. Opin. Struct. Biol.*, 2015, **33**, 61–67.
47 Y. G. Smirnova, S.-J. Marrink, R. Lipowsky and V. Knecht, *J. Am. Chem. Soc.*, 2010, **132**, 6710–6718.
48 F. de Meyer and B. Smit, *Proc. Natl. Acad. Sci. U. S. A.*, 2009, **106**, 3654–3658.
49 L. V. Chernomordik and M. M. Kozlov, *Nat. Struct. Biol.*, 2008, **15**, 675–683.
50 V. Knecht and S.-J. Marrink, *Biophys. J.*, 2007, **92**, 4254–4261.
51 A. Grafmüller, J. Shillcock and R. Lipowsky, *Phys. Rev. Lett.*, 2007, **98**, 218101.
52 P. M. Kasson, N. W. Kelley, N. Singhal, M. Vrljic, A. T. Brunger and V. S. Pande, *Proc. Natl. Acad. Sci. U. S. A.*, 2006, **103**, 11916–11921.
53 R. Blumenthal, M. J. Clague, S. R. Durell and R. M. Epand, *Chem. Rev.*, 2003, **103**, 53–70.
54 V. S. Markin and J. P. Albanesi, *Biophys. J.*, 2002, **82**, 693–712.
55 T. Mukhina, A. Hemmerle, V. Rondelli, Y. Gerelli, G. Fragneto, J. Daillant and T. Charitat, *J. Phys. Chem. Lett.*, 2019, **10**, 7195–7199.
56 A. Hemmerle, L. Malaquin, T. Charitat, S. Lecuyer, G. Fragneto and J. Daillant, *Proc. Natl. Acad. Sci. U. S. A.*, 2012, **109**, 19938–19942.
57 J. Pan, T. T. Mills, S. Tristram-Nagle and J. F. Nagle, *Phys. Rev. Lett.*, 2008, **100**, 198103.
58 W. N. Everett and M. A. Bevan, *Soft Matter*, 2014, **10**, 332–342.
59 S. L. Veatch, I. Polozov, K. Gawrisch and S. L. Keller, *Biophys. J.*, 2004, **86**, 2910–2922.
60 F. Szoka Jr and D. Papahadjopoulos, *Annu. Rev. Biophys.*, 1980, **9**, 467–508.
61 J. Yuan, C. Hao, M. Chen, P. Berini and S. Zou, *Langmuir*, 2013, **29**, 221–227.
62 D. C. Prieve and N. A. Frej, *Langmuir*, 1990, **6**, 396–403.
63 M. A. Bevan and D. C. Prieve, *J. Chem. Phys.*, 2000, **113**, 1228–1236.
64 H.-J. Wu and M. A. Bevan, *Langmuir*, 2005, **21**, 1244–1254.
65 F. Cao, J. Wu, Y. Li and T. Ngai, *Langmuir*, 2019, **35**, 8910–8920.
66 W. Liu, Z. Zhao, J. Zhong, P. W. F. Yeung, J. Wu, Y. Li, H. Jiang, Y. Zhu and T. Ngai, *Chem. Sci.*, 2025, **16**, 16625–16637.
67 J. Wu, W. Liu and T. Ngai, *Soft Matter*, 2023, **19**, 4611–4627.
68 B. Wang, S. M. Anthony, S. C. Bae and S. Granick, *Proc. Natl. Acad. Sci. U. S. A.*, 2009, **106**, 15160–15164.
69 C. Manzo, J. A. Torreno-Pina, P. Massignan, G. J. Lapeyre Jr, M. Lewenstein and M. F. Garcia Parajo, *Phys. Rev. X*, 2015, **5**, 011021.
70 G. P. Pattnaik and H. Chakraborty, *Vitamins and hormones*, Elsevier, 2021, vol. 117, pp. 133–155.
71 H. Himeno, N. Shimokawa, S. Komura, D. Andelman, T. Hamada and M. Takagi, *Soft Matter*, 2014, **10**, 7959–7967.
72 T. J. McIntosh and S. A. Simon, *Annu. Rev. Biophys. Biomol. Struct.*, 1994, **23**, 27–51.
73 R. Rand and V. Parsegian, *Biochim. Biophys. Acta Rev. Biomembr.*, 1989, **988**, 351–376.
74 C. S. Poojari, K. C. Scherer and J. S. Hub, *Nat. Commun.*, 2021, **12**, 6594.
75 S. Aeffner, T. Reusch, B. Weinhausen and T. Salditt, *Proc. Natl. Acad. Sci. U. S. A.*, 2012, **109**, E1609–E1618.
76 T. Kumarage, S. Gupta, N. B. Morris, F. T. Doole, H. L. Scott, L.-R. Stingaciu, S. V. Pingali, J. Katsaras, G. Khelashvili and M. Doktorova, *Nat. Commun.*, 2025, **16**, 7024.
77 R. F. de Almeida, L. M. Loura and M. Prieto, *Chem. Phys. Lipids*, 2009, **157**, 61–77.
78 R. F. De Almeida, J. Borst, A. Fedorov, M. Prieto and A. J. Visser, *Biophys. J.*, 2007, **93**, 539–553.
79 L. s. M. Loura, A. Fedorov and M. Prieto, *Biochim. Biophys. Acta Biomembr.*, 2001, **1511**, 236–243.
80 F. M. Goñi, A. Alonso, L. A. Bagatolli, R. E. Brown, D. Marsh, M. Prieto and J. L. Thewalt, *Biochim. Biophys. Acta Mol. Cell Biol. Lipids*, 2008, **1781**, 665–684.
81 R. F. De Almeida, A. Fedorov and M. Prieto, *Biophys. J.*, 2003, **85**, 2406–2416.
82 R. F. De Almeida, L. M. Loura, A. Fedorov and M. Prieto, *J. Mol. Biol.*, 2005, **346**, 1109–1120.